First example of erbium triple-stranded helicate displaying SMM behaviour

Adam Gorczyński,[a] Maciej Kubicki,[a] Dawid Pinkowicz,*[,b] Robert Pełka,[c] Violetta Patroniak*[,a] and Robert Podgajny*[,b]

[a] *Faculty of Chemistry, Adam Mickiewicz University, Umultowska 89b, 61614 Poznań, Poland*
[b]*Faculty of Chemistry, Jagiellonian University, Ingardena 3, 30-060 Kraków, Poland.*
[c]*H. Niewodniczański Institute of Nuclear Physics Polsih Academy of Sciences, Radzikowskiego 152, 31-342 Kraków, Poland.*

Supporting information

Table of contents

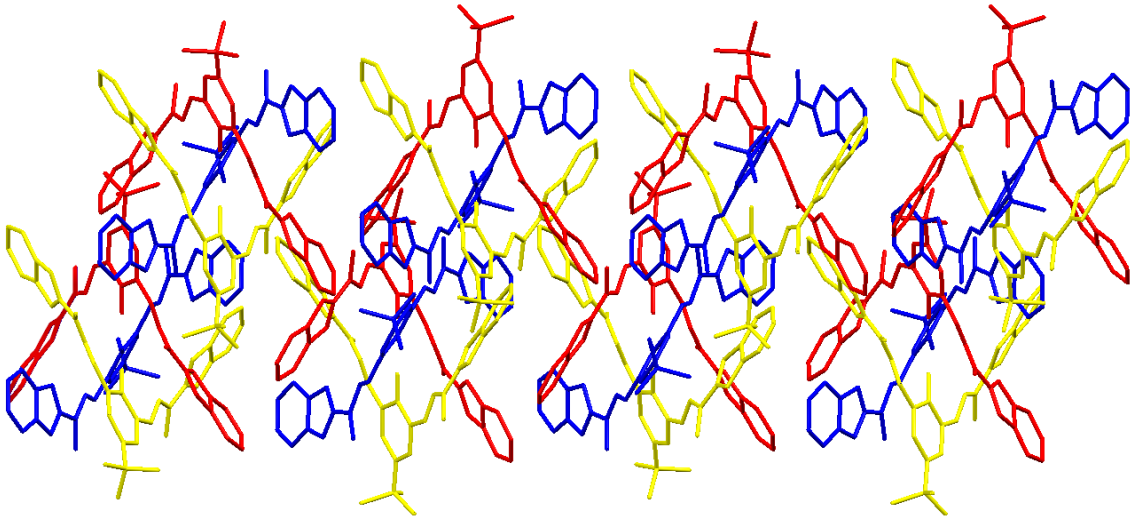

Fig. S1. Crystal packing along b axis; helical species are equally distributed between Δ and Λ isomers in ΔΔΛΛ fashion along C_3-helical axis. Hydrogen atoms, counterions and metal centres have been omitted for clarity.

Determination of CF Parameters in the Lanthanide Complexes.

The approach depends crucially on the coordination number (CN) of the geometry of the coordination sphere of the lanthanide ion. Crystallographic analysis of compounds **1**, **2**, **3**, **4**, **5**, and **6** revealed that all of them comprise isostructural homonuclear dimers with constituent trivalent lanthanide ions with CN=9 and the coordination geometry of a distorted tricapped trigonal prism (TTP, D_{3h}). The top and base faces of the prism corresponding to the first lanthanide ion Ln_1^{3+} are taken by three symmetry related atoms N1 and O1, respectively. The capping of the prism comprises three symmetry related N2 atoms. The TTP coordination sphere of the second lanthanide ion Ln_2^{3+} in the dimer shares the base face of O1 atoms with the former one, the top face is made-up of a threesome of N3 atoms, while the capping comprises three symmetry related N4 atoms. Both coordination spheres share a threefold axis going through the lanthanide centers. The third versor $\hat{e}_{\eta 1}$ of the local orthogonal right-handed coordinate frame of Ln_1^{3+} is chosen along the threefold axis and pointing toward the TTP top face. The second versor $\hat{e}_{\xi 1}$ is obtained by projecting the vector $\vec{r}_{O1} + \vec{r}_{N1}$ onto the plane perpendicular to the third versor $\hat{e}_{\eta 1}$ and normalizing the projection, where *r*'s denote the position vectors of the corresponding atoms relative to the central Ln_1^{3+} ion . And finally the first versor of the coordinate frame is calculated as the cross product of the two former ones: $\hat{e}_{\zeta 1} = \hat{e}_{\xi 1} \times \hat{e}_{\eta 1}$. Analogously, we define the local coordinate frame of Ln_2^{3+} replacing the vector $\vec{r}_{O1} + \vec{r}_{N1}$ by $\vec{r}_{O1} + \vec{r}_{N3}$. Figure S2 shows the crystallographically truthful picture of both the coordination spheres with their local frames.

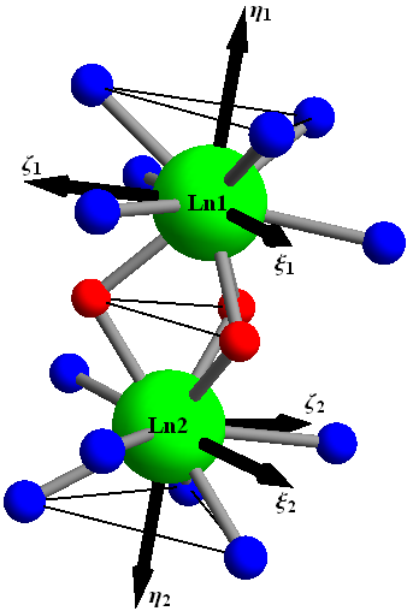

Figure S2: Crystallographically truthful picture of the dinuclear lanthanide complex with the local frames used in the calculations. Color code: blue – N, red – O, green - Ln.

The Hamiltonian pertinent to the present systems under external magnetic field is $H = H_Z + H_{CF} + H_{SE}$. The first term accounts for the Zeeman effect. For two Ln^{3+} ions in the dimer it reads

$$H_Z = \mu_B (J_{Ln1} \cdot g_{Ln1} + J_{Ln2} \cdot g_{Ln2}) \cdot H$$

where μ_B is the Bohr magneton and ***H*** denotes the external magnetic field. The total magnetic moment operator $\mu = -\mu_B (J_{Ln1} \cdot g_{Ln1} + J_{Ln2} \cdot g_{Ln2})$ is used in the corresponding $|J_1 J_{1z}; J_2 J_{2z}\rangle$ representation. The components of both g_{Ln1} and g_{Ln2} of which we assume to be diagonal and

isotropic were assumed to be equal $g_{Ln1} = g_{Ln2} = g\ diag(1,1,1)$ (quasi-symmetric approximation, see text below) and varied during the fitting procedure. The second term corresponds to the crystal field (CF) interaction, which is expressed in the framework of the extended operator equivalent approach[1-3]. Following the notation by Altshuler and Kozyrev[3], the ligand field part of the Hamiltonian is written as

$$H_{CF} = \sum_{2,4,6} \sum_{q=0}^{k} B_{1k}^{q} O_{1k}^{q} + B_{2k}^{q} O_{2k}^{q}$$

The coefficients B_{1k}^{q} and B_{2k}^{q} are the parameters to be determined. The O_{ik}^{q} (i=1,2) operators are polynomials of the total angular momentum operators J_{iz}, J_{i+}, and J_{i-} defined in the local coordinate system of each ion (and their definitions are given in the Appendix for instant reference). Because the angles and distances in the coordination spheres of both lanthanide ions in the dimer are all comparable we decide to take here a simplifying assumption that the crystal field of both ions is identical in their corresponding local frames, so it is described by the same set of parameters $B_{1k}^{q} = B_{2k}^{q} = B_{k}^{q}$. We call it a quasi-symmetrical approximation as the local frames of the lanthanide ions are not equivalent. This assumption reduces greatly the number of free parameters to be determined. The operator equivalents O_{ik}^{q} do not include the operator equivalent coefficients or the radial factors $\langle r^k \rangle$. Both factors are included in the parameters B_{k}^{q}, which restricts their application to a single *J*-manifold. The coefficients are conversed into another set of parameters $A_k^q \langle r^k \rangle$ (more commonly used in the literature) using the formula

$$B_k^q = A_k^q \langle r^k \rangle \langle J || \alpha_k || J \rangle$$

where the last factor are the operator-equivalent coefficients. They relate the angular momentum operators to the potential operators and depend on the ion and the coupling scheme assumed (e.g. *L*-*S* or intermediate). Their values tabulated for all lanthanide ions in the *L*-*S* scheme can be found in ref. 3.

The last component of the total Hamiltonian H_{SE} is to account for the superexchange coupling between the lanthanide ions mediated through the phenoxo bridges. The coupling should be taken between the corresponding spin operators. If we can neglect mixing of the multiplets with different *J* quantum numbers, so that only the matrix elements within the subspace of wave functions corresponding to the ground term value of *J* are taken into account, the spin operator S can be projected onto the total angular momentum operator J. Equations $L + S = J$ and $L + 2S = gJ$ imply that this projection is $S = (g - 1)$. We further assume that the superexchange coupling between the lanthanide ions is isotropic so the Hamiltonian H_{SE} reads

$$H_{SE} = -2J(g-1)^2 J_{Ln1} \cdot J_{Ln2}$$

With an arbitrary choice of a set of B_k^q coefficients and a finite external field, the Hamiltonian H is diagonalized. The determination of a full set of eigenvalues and eigenfunctions permits the calculation of the magnetic molar susceptibility together with the isothermal magnetization. This is performed using the generalized van Vleck formalism

$$\chi = \frac{N}{3k_B T Z_0} \sum_{n,i} \left[\sum_{j} \left| \langle \varphi_{n,i} \left| \mu \right| \varphi_{n,j} \rangle \right|^2 - 2k_B T \sum_{j,m \neq n} \frac{\left| \langle \varphi_{n,i} \left| \mu \right| \varphi_{m,j} \rangle \right|^2}{E_n - E_m} \right] exp\left(- \frac{E_n}{k_B T} \right)$$

$$M = \frac{N}{Z_H}\sum_k \langle \psi_k \left| \mu \right| \psi_k \rangle exp\left(- \frac{E_k(H)}{k_B T} \right)$$

where $Z_0 = \sum_n d_n exp\left(- E_n / k_B T \right)$, and $Z_H = \sum_k exp\left(- E_k(H) / k_B T \right)$. Here $\varphi_{n,i}$ denote the d_n-fold degenerate eigenfunctions with energy E_n in the absence of magnetic field, whereas the eigensystem $\{\psi_k, E_k(H)\}$ was calculated assuming the nonzero external magnetic field $\boldsymbol{H}$. The three principal values of the magnetic susceptibility are denoted χ_x, χ_y, χ_z. The observed molar magnetic susceptibility of powder sample is the following average

$$\bar{\chi} = \frac{1}{3}(\chi_x + \chi_y + \chi_z)$$

.

The magnetic moment per molecule measured on the powder sample was calculated for an array of 13 independent applied field orientations filling uniformly the total solid angle . The number of these orientations was chosen to obtain a good balance between accuracy of calculated values and time taken by the calculation.

Besides the interactions incorporated in the Hamiltonian *H*, for some of the compounds it turned out that the fitting quality of the susceptibility data was much enhanced at the lowest temperatures by accounting for the intermolecular interaction. It was introduced in an approximate way within the framework of the molecular field theory. The resultant molar powder susceptibility of a compound was calculated as

$$\bar{\chi} = \frac{\bar{\chi}_0}{1 - zJ'\bar{\chi}_0 / (N_A g_J^2 \mu_B^2)}$$

where $\bar{\chi}_0$ denotes the molar susceptibility of an isolated dimer, z is the number of nearest neighbors, and J' is the intermolecular coupling constant.

Fitting was carried out with the help of a specially designed procedure prepared within *Mathematica8.0* environment. Two test functions to be minimized were used. The first test function was the relative mean-square (r.m.s.) deviation from the measured χT values:

$$\sigma_{\chi T} = \frac{\sum_{i=1}^{N_{\chi T}} \left[(\bar{\chi}_i T)_{theor} - (\bar{\chi}_i T)_{exp} \right]^2}{\sum_{i=1}^{N_{\chi T}} (\bar{\chi}_i T)_{exp}^2}$$

where $N_{\chi T}$ denotes the number of experimental points. The second one, being more time consuming, was extended to include the r.m.s. deviation from the measured M values defined as follows

$$\sigma_M = \frac{\sum_{j=1}^{N_M} \left[\bar{M}_{j\,theor} - \bar{M}_{j\,exp} \right]^2}{\sum_{j=1}^{N_M} \bar{M}_{j\,exp}^2}$$

where N_M denotes the number of experimental magnetization points. The first test function was used in the first step of fitting procedure to find good starting values of the parameters. The extended test function was employed in the final step. To account for the imbalance between the number and temperature distribution of susceptibility and magnetization points, usually a simple weighted combination $\sigma = x\sigma_M + (1-x)\sigma_{\chi T}$ was used with $0.25<x<0.3$. Because the lanthanide site is expected to be of low symmetry (distorted TTP geometry) no initial assumptions should be made as to the parameters. On the other hand, the many-dimensional fits where only powder data are available will be of poor reliability. To overcome that problem the initial calculations were performed assuming a high symmetry Ansatz corresponding to ideal TTP geometry with only six nonzero crystal field parameters $A_2^0\langle r^2\rangle$, $A_4^0\langle r^4\rangle$, $A_4^3\langle r^4\rangle$, $A_6^0\langle r^6\rangle$, $A_6^3\langle r^6\rangle$, and $A_6^6\langle r^6\rangle$. Such a treatment is justified if one looks on the resulting parameter sets as the effective ones. Unfortunately, this strategy was not successful for all the complexes. For **1** and **2** the crystal field parameter set has been fully extended. As mentioned above, the presented model is based on the quasi-symmetrical approximation for the lanthanide homonuclear dimer. In reality, the crystal-field parameters corresponding to both the lanthanide ions may well differ. Although this assumption is crucial for the plausibility of the calculation it may cause and it does that some of the best-fit crystal-field parameters take on greatly enhanced values. Nevertheless, we believe that the proposed model gives an effective description reproducing satisfactorily available experimental data and reflecting approximate energy spectra of the constituent lanthanides.

Detailed DC magnetic properties

Table S1. The collection of values of average Lande factor g_{av}, $\chi_M T$ products at 300 K and magnetization of M_{sat} at 70 kOe together with the expected values.

Compound, Ln^{3+}	Ground state term	g_{theor}	g_{exp}	$\chi T_{theor,\ 300\ K}$ / $cm^3 \cdot K \cdot mol^{-1}$	$\chi T_{exp,300\ K}$ / $cm^3 \cdot K \cdot mol^{-1}$	$M_{sat,theor}$ / $N_A\mu_B$	$M_{(70\ kOe)}$ / $N_A\mu_B$
1, Tb^{3+}	$^7F_6$	3/2	1.54(3)	23.62	24.60	17.94	13.02
2, Dy^{3+}	$^6H_{15/2}$	4/3	1.386(7)	28.33	29.44	19.92	14.21
3, Ho^{3+}	$^5I_8$	5/4	1.22(1)	28.12	26.35	19.90	11.90
4, Er^{3+}	$^4I_{15/2}$	6/5	1.228(3)	22.95	23.74	17.89	11.78
5, Tm^{3+}	$^3H_6$	7/6	1.168(8)	14.29	13.02	13.88	3.55
6, Yb^{3+}	$^2F_{7/2}$	8/7	1.092(4)	5.14	4.54	7.88	3.12

Table S2. Best Fit Crystal Field Parameters (CFP) in the Quasi-Symmetrical Approximation.

CFP [cm^{-1}]	**1**	**2**	**3**	**4**	**5**	**6**
$A_2^0\langle r^2\rangle$	-365(28)	-34(4)	164(22)	139(9)	-510(5)	-119(4)
$A_2^1\langle r^2\rangle$	107(13)	38(7)				173(5)
$A_2^2\langle r^2\rangle$	-7(1)	50(7)				-481(14)
$A_4^0\langle r^4\rangle$	117(14)	-430(11)	-13(2)	-152(9)	-548(6)	-767(20)
$A_4^1\langle r^4\rangle$	747(51)	172(34)				-325(12)
$A_4^2\langle r^4\rangle$	-633(40)	73(24)				508(17)
$A_4^3\langle r^4\rangle$	175(21)	660(40)	621(93)	578(27)	-197(18)	288(10)
$A_4^4\langle r^4\rangle$	-231(22)	1039(12)				-316(9)
$A_6^0\langle r^6\rangle$	1200(101)	454(41)	-49(8)	417(11)	-441(7)	-114(4)
$A_6^1\langle r^6\rangle$	-202(29)	2618(47)				100(3)
$A_6^2\langle r^6\rangle$	1872(199)	-189(44)				100(3)
$A_6^3\langle r^6\rangle$	-147(18)	-1150(126)	1521(134)	-1589(60)	-99(10)	99(4)
$A_6^4\langle r^6\rangle$	333(44)	448(66)				101(4)
$A_6^5\langle r^6\rangle$	276(39)	665(41)				100(3)
$A_6^6\langle r^6\rangle$	333(26)	125(10)	-2.5(5)	-151(5)	1079(14)	104(4)

Magnetic properties of 1

Figure S3 (left) shows the $\chi_M T(T)$ and $M(H)$ characteristics for the powder sample of **1**. The $\chi_M T(T)$ curve displays a smooth increase with decreasing temperature starting at the value of 24.60 $cm^3 \cdot K \cdot mol^{-1}$ for 300 K and attains a maximum of 31.38 $cm^3 \cdot K \cdot mol^{-1}$ at 18.5 K. The increasing χT values on lowering temperature are somewhat surprising, as what one would expect is damping the signal due to the depopulation of the crystal-field split levels. The observed contrary behavior points to the presence of a substantial ferromagnetic super-exchange coupling between the constituent Tb^{3+} ions through the phenoxo-bridges. Upon further cooling the signal drops to 23.29 $cm^3 \cdot K \cdot mol^{-1}$ at 1.8 K. The relevant $M(H)$ curve at T = 1.8 K increase strongly up to H = 4.1 kOe, then the slope becomes far less steep to reach a slow steady increasing tendency above 12 kOe. The magnetization value of 13.02 $N_A\mu_B$ at 70 kOe is much smaller than 17.94 $N_A\mu_B$ expected on the basis of the free-ion approximation calculated at the same values of temperature and external magnetic field. The low field behavior is consistent with ferromagnetic ground state. The further slow and unaccomplished saturation of magnetization indicate a significant anisotropy, which is slowly overcome by increasing magnetic field. This indicates that the interactions between the Tb^{3+} ions as well as the crystal field effects play a crucial role in defining the magnetic properties of **1** at low temperatures. The non-collinear character of the reduced magnetization $M(H/T)$ curves confirms a presence of magnetic anisotropy in **1** (Figure S3 right)

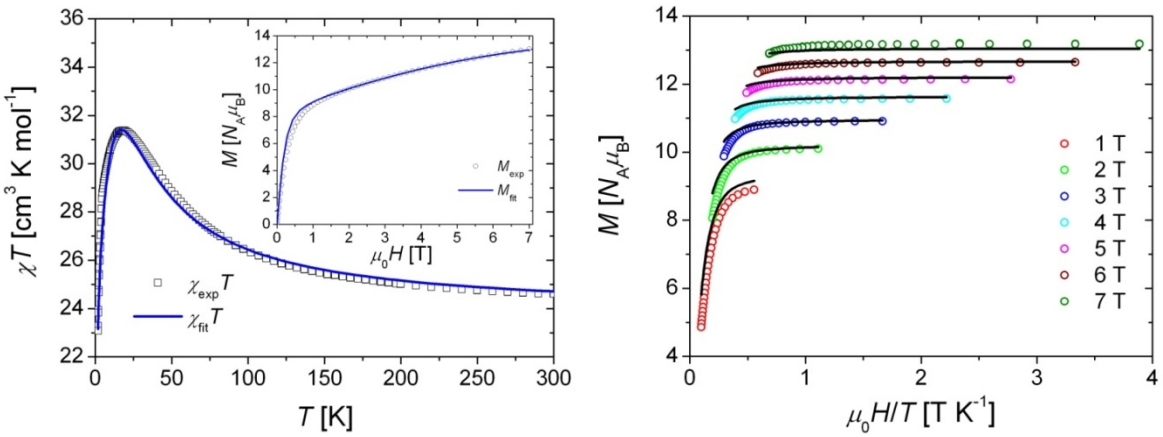

Figure S3: Temperature dependence of χT for **1** (left). Inset: Isothermal magnetization at T=1.8 K. Magnetization vs. reduced magnetic field for **1** for seven indicated applied field values (right). The experimental points form separate branches indicating the presence of magnetic anisotropy.

The ground state arising from the $4f^8$ configuration of the Tb^{3+} ion is $^7F_6$. The dimension of its ground-state subspace is hence 13. The theoretically predicted value of the Landé factor is 3/2(=1.5). The model system comprises two exchange coupled Tb^{3+} centers. The dimension of the state space of the dimer, where the calculations are performed, is hence 13^2=169. The fit to the experimental data required taking into account the full set of crystal-field parameters, as all trials to confine the model to the high symmetry case were unsuccessful. The best fit was found for the crystal field parameters listed in Table S2, and $g_{Tb} = 1.54(3), J = +1.4(2), zJ' = -0.008(1)$ (the CF parameters and the exchange couplings are always given in cm^{-1} everywhere in the text. The r.m.s. deviation obtained for the susceptibility and magnetization data are $\sigma_{\chi T}$=1.8·10^{-4} and σ_M=8.0·10^{-4}, respectively.

2b. Magnetic properties of 2

Figure S4 (left) shows the $\chi_M T(T)$ and $M(H)$ characteristics for the powder sample of **2**. As temperature lowers the $\chi_M T$ decreases from a value of 29.44 $cm^3 \cdot K \cdot mol^{-1}$ at room temperature down to 22.81 $cm^3 \cdot K \cdot mol^{-1}$ at 2 K. The decrease is smooth down to *ca*. 100 K then becomes more steep. This tendency is only disrupted by a small step-like feature at about 8 K. The course of $\chi_M T(T)$ curve may be attributed to the gradual depopulation of the crystal-field split levels, combined with weak super-exchange coupling between the constituent Dy^{3+} ions through the phenoxo-bridges and intermolecular interactions operating in low temperatures. Below 2 K it steeply rises attaining a value of 24.17 $cm^3 \cdot K \cdot mol^{-1}$ at 1.8 K. The latter feature may probably be attributed to the onset of intermolecular interactions. The relevant $M(H)$ curve at 2 K increase strongly up to H = 4.6 kOe, then the slope becomes far less steep. At 40 kOe the inflection point occur and the value 14.21 $N_A\mu_B$ is reached at 70 kOe, being considerably lower than the value of 19.92 $N_A\mu_B$ calculated within the free-ion approximation at the corresponding values of temperature and magnetic field. The low field behavior is consistent with ferromagnetic ground state. The further slow and unaccomplished saturation of magnetization indicate a strong anisotropy, which is slowly overcome by increasing magnetic field. The inflection point at 40 kOe can be interpreted in terms of changes in magnetic ground state. This indicates that the interactions between the Dy^{3+} ions as well as the crystal field effects play a crucial role in defining the magnetic properties of **2** at low temperatures. The non-collinear character of the reduced magnetization $M(H/T)$ curves confirms a presence of magnetic anisotropy in **2** (Figure. 4 right)

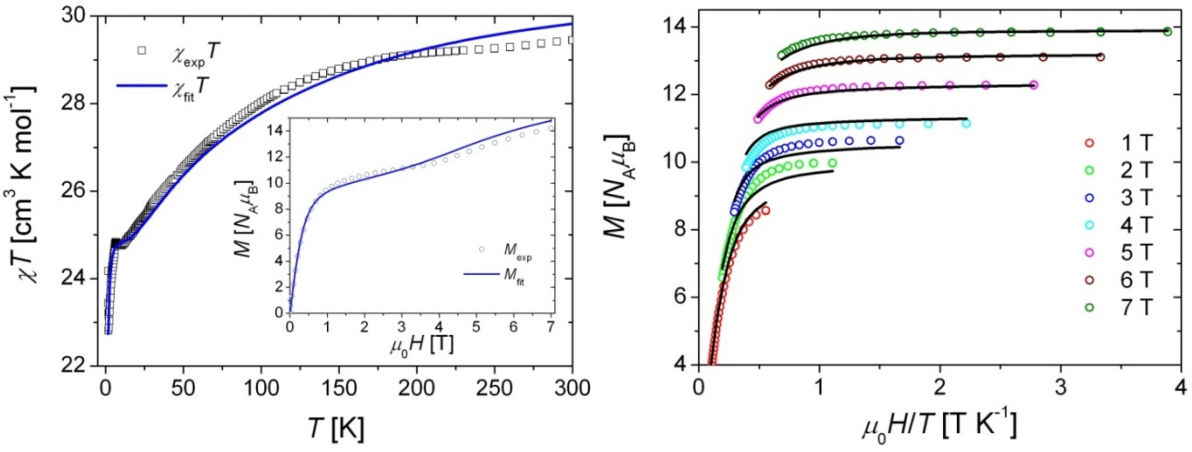

Figure S4. Temperature dependence of χT for **2** (left). Inset: Isothermal magnetization at T=1.8 K. Magnetization vs. reduced magnetic field for **2** for seven indicated applied field values (right). The experimental points form separate branches indicating the presence of magnetic anisotropy.

The ground state arising from the $4f^9$ configuration of the Dy^{3+} ion is $^6H_{15/2}$. The dimension of its ground-state subspace is hence 16. The theoretically predicted value of the Landé factor is 4/3(≈1.3). The model system comprises two exchange coupled Dy^{3+} centers. The dimension of the state space of the dimer, where the calculations are performed, is hence 16^2=256. The fit to the experimental data required taking into account the full set of crystal-field parameters, as all trials to confine the model to the high symmetry case were unsuccessful. The best fit was found for the crystal field parameters listed in Table S2, and $g_{Dy} = 1.386(7), J = +0.05(5), zJ' = -0.01(1)$. The r.m.s. deviation obtained for the susceptibility and magnetization data are $\sigma_{\chi T}$=7.0·10^{-5} and σ_M=6.6·10^{-4}, respectively.

Magnetic properties of 3

Figure S5 (left) shows the $\chi_M T(T)$ and $M(H)$ characteristics for the powder sample of **3**. As temperature lowers the $\chi_M T$ decreases from a value of 26.35 $cm^3 \cdot K \cdot mol^{-1}$ at room temperature down to 9.08 $cm^3 \cdot K \cdot mol^{-1}$ at 1.8 K. The decrease is smooth down to *ca*. 50 K then becomes strongly steep. The course of $\chi_M T(T)$ curve may be attributed to the gradual depopulation of the crystal-field split levels, combined with weak antiferromagnetic super-exchange coupling between the constituent Ho^{3+} ions through the phenoxo-bridges and intermolecular interactions operating in low temperatures. The relevant $M(H)$ curve at 2 K increase up to H = 11 kOe, then the slope becomes less steep to reach the value 11.90 $N_A\mu_B$ at 70 kOe, being considerably lower than the value of 19.90 $N_A\mu_B$ calculated within the free-ion approximation at the corresponding values of temperature and magnetic field. The low field increase in $M(H)$ is weaker compared to **1**, **2** or **4** (*see below*) which could be indicative to a contribution of antiferromagnetic ground state. Unaccomplished saturation of magnetization indicate a strong anisotropy, which is slowly overcome by increasing magnetic field. This indicates that the interactions between the Ho^{3+} ions as well as the crystal field effects play a crucial role in defining the magnetic properties of **3** at low temperatures. The non-collinear character of the reduced magnetization $M(H/T)$ curves confirms a presence of magnetic anisotropy in **3** (Figure S5 right).

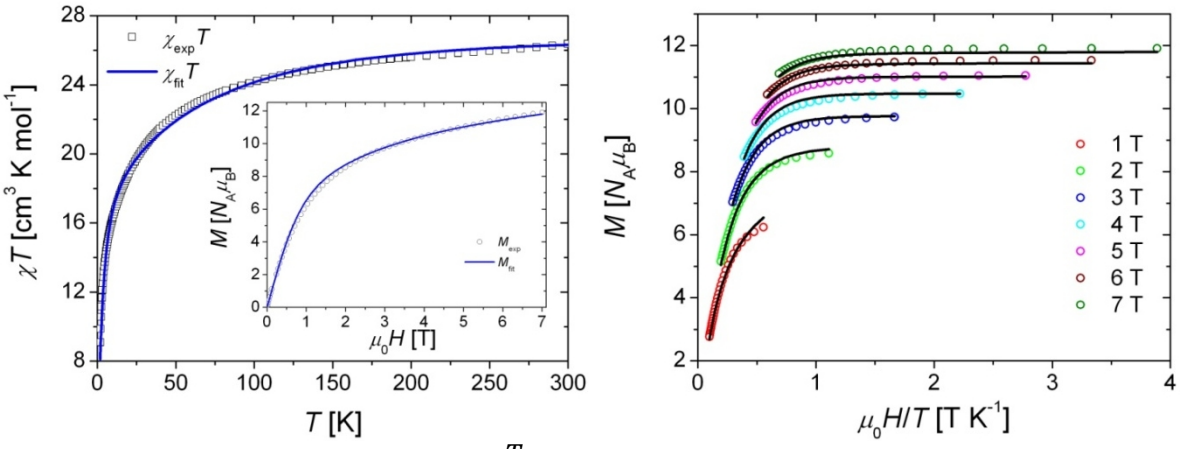

Figure S5 Temperature dependence of χT for **3** (left). Inset: Isothermal magnetization at T=1.8 K. Magnetization vs. reduced magnetic field for **3** for seven indicated applied field values (right). The experimental points form separate branches indicating the presence of magnetic anisotropy.

The ground state arising from the $4f^{10}$ configuration of the Ho^{3+} ion is $^5I_8$. The dimension of its ground-state subspace is hence 17. The theoretically predicted value of the Landé factor is 5/4(=1.25). The model system comprises two exchange coupled Ho^{3+} centers. The dimension of the state space of the dimer, where the calculations are performed, is hence 17^2=289. The fit to the experimental data was satisfactory on confining the model to the high symmetry case. The best fit was found for the crystal field parameters listed in Table S2, and $g_{Ho} = 1.22(1)$, $J = -0.11(2)$, $zJ' = -0.025(7)$. The r.m.s. deviation obtained for the susceptibility and magnetization data are $\sigma_{\chi T}$=2.5·10^{-4} and σ_M=7.0·10^{-5}, respectively.

Magnetic properties of 4

Figure S6 (left) shows the $\chi_M T(T)$ and $M(H)$ characteristics for the powder sample of **4**. The $\chi_M T(T)$ decrease smoothly from 23.74 $cm^3 \cdot K \cdot mol^{-1}$ in 300 K reaching a minimum of 21.23 $cm^3 \cdot K \cdot mol^{-1}$ at 24.0 K then increase strongly towards 27.44 $cm^3 \cdot K \cdot mol^{-1}$ at 1.8 K. Such behavior is indicative for depopulation of the crystal-field split levels combined in lower temperature with ferromagnetic super-exchange coupling between the constituent Er^{3+} ions through the phenoxo-bridges and intermolecular interactions. The relevant $M(H)$ curve at T = 1.8 K increase strongly up to H = 2.7 kOe, then the slope becomes far less steep to reach a slow steady increasing tendency above 10 kOe. The magnetization value of 11.78 $N_A\mu_B$ at 70 kOe is much smaller than 17.89 $N_A\mu_B$ expected on the basis of the free-ion approximation calculated at the same values of temperature and external magnetic field. The low field behavior is consistent with ferromagnetic ground state. The further slow and unaccomplished saturation of magnetization indicate a strong anisotropy, which is slowly overcome by increasing magnetic field. This indicates that the interactions between the Er^{3+} ions as well as the crystal field effects play a crucial role in defining the magnetic properties of **4** at low temperatures. The non-collinear character of the reduced magnetization $M(H/T)$ curves confirms a presence of magnetic anisotropy in **4** (Figure S6 right)

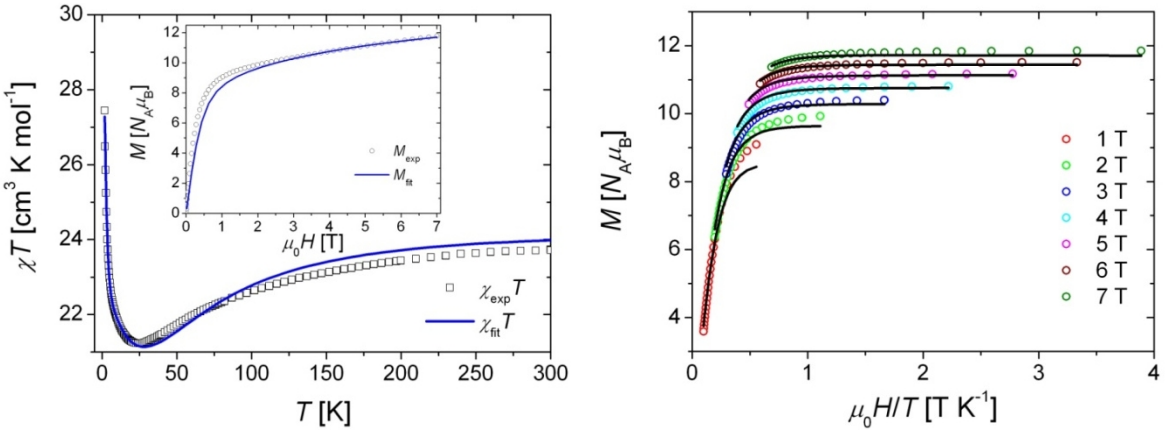

Figure S6 Temperature dependence of χT for **4** (left). Inset: Isothermal magnetization at T=1.8 K. Magnetization vs. reduced magnetic field for **4** for seven indicated applied field values (right). The experimental points form separate branches indicating the presence of magnetic anisotropy.

The ground state arising from the $4f^{11}$ configuration of the Er^{3+} ion is $^4I_{15/2}$. The dimension of its ground-state subspace is hence 16. The theoretically predicted value of the Landé factor is 6/5(=1.2). The model system comprises two exchange coupled Er^{3+} centers. The dimension of the state space of the dimer, where the calculations are performed, is hence 16^2=256. The fit to the experimental data was satisfactory on confining the model to the high symmetry case. The best fit was found for the crystal field parameters listed in Table S3, and $g_{Er} = 1.228(3)$, $J = +1.8(1)$, $zJ' = +0.019(1)$. The r.m.s. deviation obtained for the susceptibility and magnetization data are $\sigma_{\chi T}$=5.1·10^{-5} and σ_M=1.9·10^{-4}, respectively.

Magnetic properties of 5

Figure S7 shows the $\chi_M T(T)$ and $M(H)$ characteristics for the powder sample of **5**. As temperature lowers the $\chi_M T$ decreases from a value of 13.02 $cm^3 \cdot K \cdot mol^{-1}$ at room temperature down to 0.64 $cm^3 \cdot K \cdot mol^{-1}$ at 1.8 K. The decrease is smooth down to *ca*. 50 K then becomes strongly steep. The course of $\chi_M T(T)$ curve may be attributed to the gradual depopulation of the crystal-field split levels, combined with non-negligible antiferromagnetic super-exchange coupling between the constituent Tm^{3+} ions through the phenoxo-bridges and intermolecular interactions operating in low temperatures. The relevant $M(H)$ curve at 2 K increase in almost perfectly linear manner up to *ca.* 50 kOe, then slightly diverge from this tendency, which is completely different in comparison with the $M(H)$ curves for **5**. The value 3.55 $^{N_A\mu_B}$ at 70 kOe is significantly lower than the value of 13.88 $^{N_A\mu_B}$ calculated within the free-ion approximation at the corresponding values of temperature and magnetic field. The observed tendency could be, at the first glance, indicative of significant contribution of antiferromagnetic ground state, besides the obvious contribution of crystal field parameters. In this case it is however very difficult to judge on the real balance between both contribution, as different negative values of $J_{Tm\text{-}Tm}$ could be easily obtained to produce a good reproducibility of measured data, unlike in other case under this study. The non-collinear character of the reduced magnetization $M(H/T)$ is presented in Figure S7 (right). Unlike the case of **1**-**4** all curves almost linear in the examined range.

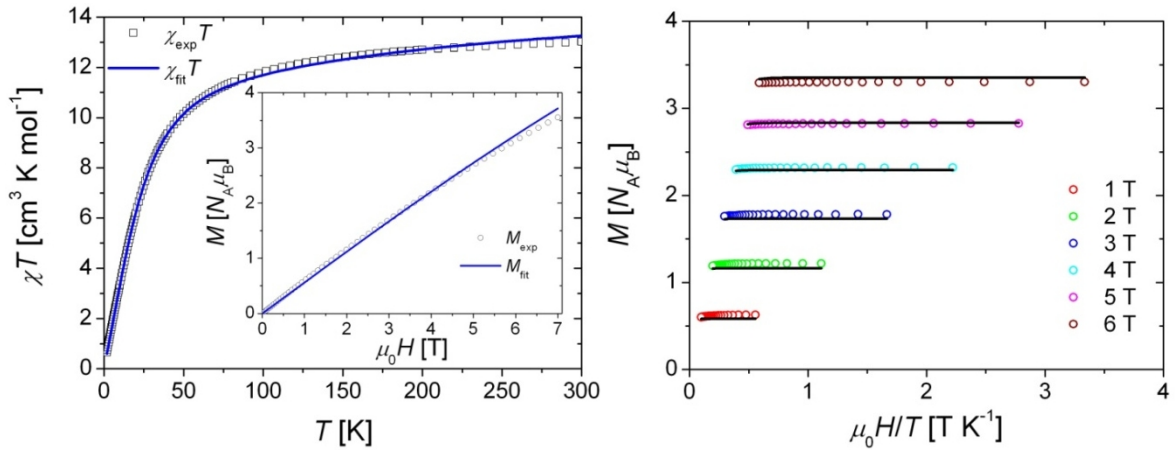

Figure S7 Temperature dependence of χT for **5** (left). Inset: Isothermal magnetization at T=1.8 K. Magnetization vs. reduced magnetic field for **5** for seven indicated applied field values (right). The experimental points form separate branches indicating the presence of magnetic anisotropy.

The ground state arising from the $4f^{12}$ configuration of the Tm^{3+} ion is $^3H_6$. The dimension of its ground-state subspace is hence 13. The theoretically predicted value of the Landé factor is 7/6(≈1.17). The model system comprises two exchange coupled Tm^{3+} centers. The dimension of the state space of the dimer, where the calculations are performed, is hence 13^2=169. The fit to the experimental data was satisfactory with confining the model to the high symmetry case. The best fit was found for the crystal field parameters listed in Table S2, and $g_{Tm} = 1.168(8), J = -0.35(5)$. The r.m.s. deviation obtained for the susceptibility and magnetization data are $\sigma_{\chi T}$=6.1·10^{-5} and σ_M=2.8·10^{-4}, respectively.

Magnetic properties of 6

Figure S8 shows the $\chi_M T(T)$ and $M(H)$ characteristics for the powder sample of **6**. As temperature lowers the $\chi_M T$ decreases from a value of 4.54 $cm^3 \cdot K \cdot mol^{-1}$ at room temperature down to 2.04 $cm^3 \cdot K \cdot mol^{-1}$ at 3.3 K. The decrease is smooth down to *ca*. 100 K then becomes more steep. Below 3.3 K the signal rises up slightly to 2.08 $cm^3 \cdot K \cdot mol^{-1}$. The course of $\chi_M T(T)$ curve may be attributed to the gradual depopulation of the crystal-field split levels, while it is rather difficult to judge on the type of super-exchange coupling between the constituent Yb^{3+} ions through the phenoxo-bridges. The relevant $M(H)$ curve at 2 K increase up to H = 15 kOe, then the slope becomes less steep to reach the value 3.12 $N_A\mu_B$ at 70 kOe, being significantly lower than the value of 7.88 $N_A\mu_B$ calculated within the free-ion approximation at the corresponding values of temperature and magnetic field. The low field increase in $M(H)$ is weaker compared to **1**, **2** or **4** (*see below*) indicating rather a contribution of antiferromagnetic ground state. Thus, again it is impossible to judge one the balance of possible contributions. Unlike the cases of **1**-**5**, the reduced magnetization $M(H/T)$ curves lies very close to each other suggesting that magnetic anisotropy is strongly reduced in **6** (Figure S8 right).

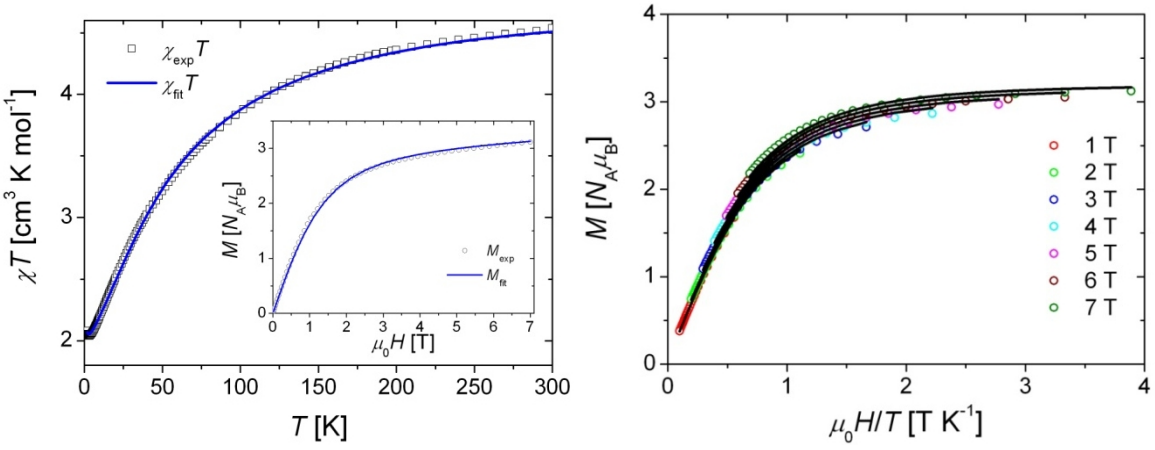

Figure S8 Temperature dependence of χT for **6** (left). Inset: Isothermal magnetization at T=1.8 K. Magnetization vs. reduced magnetic field for **6** for seven indicated applied field values (right). The experimental points form separate branches indicating the presence of magnetic anisotropy.

.

The ground state arising from the $4f^{13}$ configuration of the Yb^{3+} ion is $^2F_{7/2}$. The dimension of its ground-state subspace is hence 8. The theoretically predicted value of the Landé factor is 8/7(≈1.14). The model system comprises two exchange coupled Yb^{3+} centers. The dimension of the state space of the dimer, where the calculations are performed, is hence 8^2=64. The fit to the experimental data required taking into account the full set of crystal-field parameters, as all trials to confine the model to the high symmetry case were unsuccessful. The best fit was found for the crystal field parameters listed in Table S2, and $g_{Yb} = 1.092(4), J = +1.05(3)$. The r.m.s. deviation obtained for the susceptibility and magnetization data are $\sigma_{\chi T}$=2.9·10^{-5} and σ_M=1.1·10^{-4}, respectively.

Table S3. Extended Operator Equivalents O_k^q

k	q	O_k^q
2	0	$\frac{1}{2}(3J_z^2 - jI)$
	1	$\frac{\sqrt{6}}{4}[J_z J_+ + J_- J_z]_+$
	2	$\frac{\sqrt{6}}{4}(J_+^2 + J_-^2)$
4	0	$\frac{1}{8}(35J_z^4 - 5(6j-5)J_z^2 + 3j(j-2)I)$
	1	$\frac{\sqrt{5}}{8}[7J_z^3 - (3j+1)J_z J_+ + J_- J_z]_+$
	2	$\frac{\sqrt{10}}{16}[7J_z^2 - (j+5)I, J_+^2 + J_-^2]_+$
	3	$\frac{\sqrt{35}}{8}[J_z J_+^3 + J_-^3 J_z]_+$
	4	$\frac{\sqrt{70}}{16}(J_+^4 + J_-^4)$
6	0	$\frac{1}{16}(231J_z^6 - 105(3j-7)J_z^4 + (105j^2 - 525j + 294)J_z^2 - 5j(j^2 - 8j - 12)I)$
	1	$\frac{\sqrt{42}}{32}[33J_z^5 - 15(2j-1)J_z^3 + (5j^2 - 10j + 12)J_z J_+ + J_- J_z]_+$
	2	$\frac{\sqrt{105}}{64}[33J_z^4 - (18j+123)J_z^2 + (j^2 + 10j + 102)I, J_+^2 + J_-^2]_+$
	3	$\frac{\sqrt{105}}{32}[11J_z^3 - (3j+59)J_z J_+^3 + J_-^3 J_z]_+$
	4	$\frac{3\sqrt{14}}{64}[11J_z^2 - (j+38)I, J_+^4 + J_-^4]_+$
	5	$\frac{3\sqrt{77}}{32}[J_z J_+^5 + J_-^5 J_z]_+$
	6	$\frac{\sqrt{231}}{16}(J_+^6 + J_-^6)$

$[A,B]_+ = \frac{(AB+BA)}{2}$, $j = J(J+1)$, *and* I *– the identity operator*

Concluding remarks

The application of the generalized van Vleck formalism enabled the estimation of the CF parameters for the Ln^{3+} ions within the quasi-symmetrical approximation and the determination of the superexchange coupling constants between the constituent Ln^{3+} ions in a dimer unit in **1**, **2**, **3**, **4**, **5**, and **6**. All the compounds discussed are isostructural, so the coordination geometry of the Ln^{3+} ions is that of a distorted tricapped trigonal prism (TTP). Only for **3**, **4**, and **5** the high symmetry Ansatz corresponding to that geometry turned out to yield satisfactory results. In the remaining cases the CF parameter set had to be extended to include the full set.

References

1. K. W. H. Stevens, *Proc. Phys. Soc., London, Sect. A* 1952, **65**, 209.

2. A. Abragam, B. Bleaney, *Electron Paramagnetic Resonance of Transition Ions;* Clarendon Press: Oxford, 1970.

3. S. Altshuler, B. M. Kozyrev, *Electron Paramagnetic Resonance in Compounds of Transition Elements;* Nauka: Moscow, 1972; in Russian.